


**Mott localization in the van der Waals crystal CrI<sub>3</sub>: A GGA+DMFT study**L. Craco,<sup>1,2</sup> S. S. Carara,<sup>1</sup> Y.-C. Shao,<sup>3,4</sup> Y.-D. Chuang,<sup>3</sup> and B. Freelon<sup>4,5</sup><sup>1</sup>*Institute of Physics, Federal University of Mato Grosso, 78060-900, Cuiabá, Mato Grosso, Brazil*<sup>2</sup>*Leibniz Institute for Solid State and Materials Research Dresden, D-01069, Dresden, Germany*<sup>3</sup>*Advanced Light Source, Lawrence Berkeley National Laboratory, Berkeley, California 94720, USA*<sup>4</sup>*Department of Physics, University of Houston, Houston, Texas 77204, USA*<sup>5</sup>*Texas Center for Superconductivity, University of Houston, Texas 77204, USA* (Received 25 May 2020; revised 30 September 2020; accepted 4 November 2020; published 17 November 2020)

Using the generalized gradient approximation plus dynamical mean-field theory (GGA+DMFT) we confirm the importance of multi-orbital dynamical correlations in determining the paramagnetic insulating state of CrI<sub>3</sub>. While the ferromagnetic phase reveals weak electronic correlation effects due to strong spin-orbital polarization, the Mott insulating state of paramagnetic CrI<sub>3</sub> crystal is shown to be driven by the interplay between orbital-dependent one-electron lineshape and multi-orbital electronic interactions. To probe the paramagnetic Mott insulating state we performed x-ray absorption spectroscopy (XAS) measurements for the two structural phases of CrI<sub>3</sub>. Our study is relevant to understanding the orbital-selective electronic structure reconstruction of Mott insulators and should be applicable to other van der Waals bonded materials from bulk to the ultrathin limit.

DOI: [10.1103/PhysRevB.102.195130](https://doi.org/10.1103/PhysRevB.102.195130)**I. INTRODUCTION**

Intrinsic van der Waals magnetic materials have received growing interest [1–4] due to their potential for a wide spectrum of spintronic applications and the opportunity for the development of functional heterostructures [5]. Of particular interest is chromium triiodide (CrI<sub>3</sub>) [6], showing a layer-dependent magnetic ground state [7,8]. In this system the magnetic moments are aligned in the out-of-plane direction of each layer and antialigned in adjacent layers [5,8–11]. As a result, monolayer CrI<sub>3</sub> is ferromagnetic [12] bilayer CrI<sub>3</sub> has an antiferromagnetically ordered ground state [8] and bulk CrI<sub>3</sub> is a ferromagnetic semiconductor [11–13] with Curie temperature of  $T_C = 61$  K and band gap of approximately 1.6 eV [6]. Upon cooling, CrI<sub>3</sub> undergoes a structural phase transition around 220 K from the high-temperature monoclinic (space group  $C2/m$ ) to the rhombohedral ( $R\bar{3}$ ) low-temperature phase [14–16], see Fig. 1. It is noteworthy that CrI<sub>3</sub> displays electric field controlled magnetism [17] and strong magnetic anisotropy [14,18]. The magnetic properties of CrI<sub>3</sub> mono and bilayers can be controlled by electrostatic doping [17] or by pressure in atomically thin films [19]. Monte Carlo simulations for the Heisenberg model predicts Curie temperatures of chromium trihalides up to 90 K, which could be further increased by applying biaxial tensile strains [20]. With the main absorption peaks lying in the visible part of the spectrum, CrI<sub>3</sub> is considered to be a possible candidate for future magneto-electronic and magneto-optic applications [20].

It is now recognized that in narrow-band transition-metal oxides and halides localized moments naturally emerge in the incompletely filled  $3d$  shells of the transition metal ions [21]. This is known to be a consequence of strong electron correlation effects in the solid [22]. On general grounds narrow band

transition-metal systems often follow in the rubric of Mott-Hubbard and charge-transfer insulators [22,23] where on-site electron-electron interactions are described by Hubbard-type many-body (multiband or not) model Hamiltonians. With this in place and using a Rayleigh-Schrödinger perturbation expansion of a multiband Hubbard model, the authors of Ref. [21] derived analytic expressions for the superexchange coupling constants between Cr ions of Rb<sub>2</sub>CrCl<sub>4</sub> and the CrX<sub>3</sub> ( $X = \text{Br}, \text{Cl}, \text{I}$ ) family. Importantly, the degree of electron-electron interactions in CrCl<sub>3</sub> and CrBr<sub>3</sub> crystals have been estimated using a combination of photoemission and ultraviolet reflectance spectroscopy [23], predicting an average on-site Coulomb interaction  $U$  of  $3.45 \pm 0.25$  for CrCl<sub>3</sub> and  $2.95 \pm 0.25$  for CrBr<sub>3</sub> in good qualitative accord with the  $U$  values used in our GGA+DMFT calculations for CrI<sub>3</sub> bulk crystal [24].

Electronic structure, band gap, and magnetic properties from bulk down to single layer CrI<sub>3</sub> were investigated by different *ab initio* density functional theories (DFT) implemented within the generalized gradient approximation (GGA) and GGA+ $U$  schemes. [7,11–13,20]. These calculations correctly describe the insulating electronic state of ferromagnetic CrI<sub>3</sub>, with almost fully spin-polarized minority, spin- $\downarrow$  electronic states. Moreover, a perusal of extant GGA+ $U$  studies, which explicitly take into account the effect of local electron-electron interactions in the Cr  $3d$  shell, reveals that the on-site Coulomb interaction  $U$  for CrI<sub>3</sub> could be in the range between 1.0 and 3.9 eV [7,11,12]. However, in spite of these theoretical efforts, neither the insulating state of CrI<sub>3</sub> above  $T_C$  [1,9] nor the orbital-selective electronic structure reconstruction of paramagnetic CrI<sub>3</sub> crystal have been discussed so far. In this work we shed light onto this problem within the GGA+DMFT approximation [25], showing that

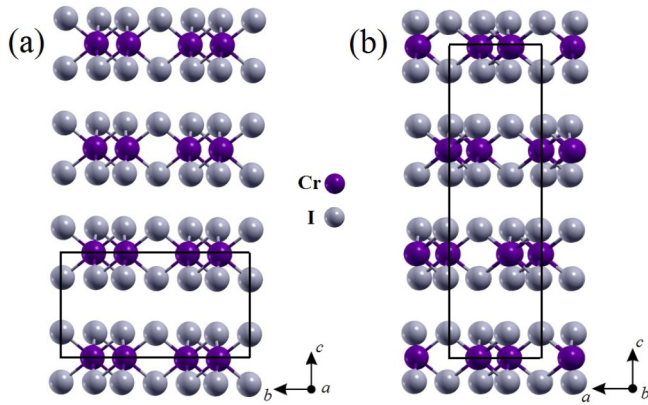


FIG. 1. Schematic representation of (a) monoclinic and (b) rhombohedral crystal structure of  $\text{CrI}_3$ . Black lines represent the unit cells.

the emergent strongly correlated electronic state is caused by large dynamical transfer of spectral weight with concomitant formation of orbital-selective localized moments in  $\text{CrI}_3$ . Similar to  $\text{BiFeO}_3$  [26] our study highlights the importance of incorporating dynamical many-particle aspects of multi-orbital (MO) electronic correlation effects within the Cr-3d orbitals to correctly derive the insulating spectra of paramagnetic  $\text{CrI}_3$ . Likewise, here we present a self-consistent many-particle study of electronic structure calculations using the GGA+DMFT approach for  $\text{CrI}_3$  crystal. We show how this can provide a consistent explanation for the more relevant electron correlation fingerprints in the unoccupied states near the Fermi level,  $E_F$ .

## II. RESULTS AND DISCUSSION

Here, the DFT calculations were performed for the normal and the spin-polarized electronic state of  $\text{CrI}_3$  using the SIESTA *ab initio* simulation package [27]. Generalized gradient approximation (GGA) in the Perdew-Burke-Ernzerhof (PBE) implementation [28] was applied as the exchange correlation functional. Norm-conserving pseudopotentials of Troullier-Martins [29] in Kleinman-Bylander nonlocal form were used to represent the ionic core potential. The Kohn-Sham orbitals [30] are expanded in a linear combination of atomic orbitals of finite range which is determined by a common confinement energy shift of 0.01 Ry [31]. The precision of the real-space grid integration is determined by an energy cutoff of 200 Ry [32]. The respective Brillouin zone is sampled by a  $10 \times 10 \times 10$  Monkhorst-Pack grid [33] for a primitive cell of bulk  $\text{CrI}_3$ . All the lattice constants were taken from Ref. [16]. Finally, the atomic positions were fully optimized until all the force components became smaller than 0.04 eV/Å. Within this, in Fig. 2 we display the band structure of ferromagnetic  $\text{CrI}_3$  bulk crystal, confirming that the electronic and magnetic properties of  $\text{CrI}_3$  are represented by the ferromagnetically ordered ground state [12]. As expected [12,34], due to intrinsic spin-polarization the degenerated bands get split, resulting in an indirect energy band gap of 0.54 and 3.23 eV for the majority (spin- $\uparrow$ ) and minority (spin- $\downarrow$ ) electrons, respectively. As seen, for the spin- $\uparrow$  electrons, the conduction band minimum

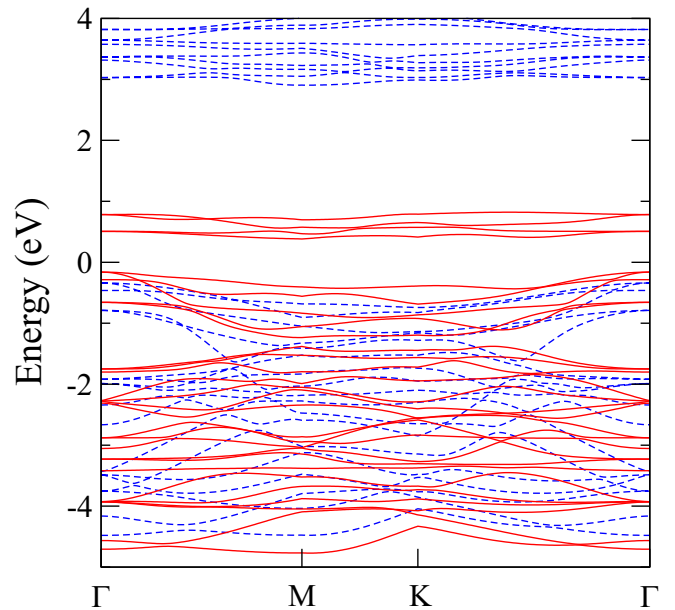


FIG. 2. GGA band structure of ferromagnetic  $\text{CrI}_3$  rhombohedral bulk crystal, with the Fermi level ( $E_F$ ) being set to zero. The solid-red and dashed-blue lines indicate, respectively, the attribution of the majority and minority spin states.

and valence band maximum are located at the  $\Gamma$  point and in the line from  $\Gamma$  to  $M$ . On the other hand, for the spin- $\downarrow$  electronic channel, the indirect band gap originates from  $M$  and  $\Gamma$  points in accord with earlier studies [34]. It is also noted that the conduction and valence band state close  $E_F$  are exclusively occupied by spin- $\uparrow$ , rendering a half-semiconducting electronic state [34] relevant to spintronic and spin photovoltaic devices based on single-spin semiconductors [12].

To provide insights for the emergent electronic reconstruction due to Mott-Hubbard localization [21] as well as the emergence of upper Hubbard bands [22] in the monoclinic and rhombohedral structural phases of paramagnetic  $\text{CrI}_3$ , we use x-ray absorption spectroscopy (XAS). The total fluorescence yield (TFY) mode of XAS spectra were recorded using the qRIXS end station at Beamline 8.0.1 at the Advanced Light Source (ALS), Lawrence Berkeley National Laboratory [35]. Commercial  $\text{CrI}_3$  samples from HQ graphene were used in the measurement. The samples were cleaved *ex situ* in the dark Ar environment to minimize the degradation before being introduced into the experimental load lock chamber. During the measurement, the photon polarization was in the horizontal plane ( $\pi$ -polarization) and the beamline energy resolution was set to 0.35 eV. The sample was oriented at 45° incidence angle relative to the surface normal. A GaAsP photodiode for TFY collection was located at 140 degrees emission angle relative to the incident x-ray beam, that roughly face to the sample surface. An open cycle cryostat with flowing liquid nitrogen (LN2) was used to cool the sample down from 300 to 80 K for temperature-dependence measurements. The XAS spectra at the Cr  $L_{2,3}$ -edge were first normalized to the incident photon flux from an upstream Au mesh and further normalization to make the pre- and post-edge spectral weight to be 0 and 1, respectively.

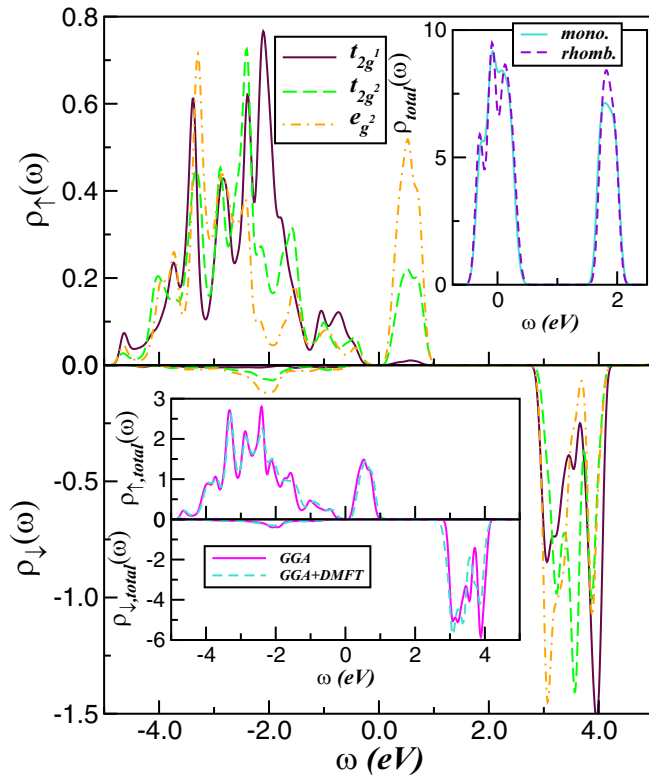


FIG. 3. Effect of ferromagnetic spin-ordering on the bare GGA orbital- and spin-resolved density of states (DOS) of rhombohedral  $\text{CrI}_3$  bulk crystal, showing strong orbital-spin polarization effects. Comparison between the total GGA and GGA+DMFT(MO-IPT) [24] DOS for the Cr  $3d$ -states of  $\text{CrI}_3$  (lower-inset), displaying weak transfer of spectral weight due to strong orbital and spin polarization. Upper inset displays the total GGA  $3d$ -DOS of monoclinic and rhombohedral crystal structure, showing similar electronic structure within the paramagnetic phase of  $\text{CrI}_3$ .

Before delving into the emergent Mott insulating state [22] of paramagnetic  $\text{CrI}_3$ , it should be noted that in earlier studies the hidden correlated electronic structure of ferromagnetic crystals has been studied [26,36,37], showing why they can be semiquantitatively understood using DFT+DMFT with sizable MO correlations. Here, we extend this aspect to characterize first the electronic properties of ferromagnetic  $\text{CrI}_3$  and its link to spin and orbital polarization. To begin with, in the two main panels of Fig. 3 we show the orbital-resolved GGA density of states (DOS) of the majority ( $\uparrow$ ) and minority ( $\downarrow$ ) spin channels of ferromagnetic  $\text{CrI}_3$ . Owing to the octahedral environment of the Cr sites, the  $3d$  (magnetic or not) states are split in low-lying  $t_{2g}$  and high-lying  $e_g$  groups. These two groups are composed by twofold-degenerate  $t_{2g}^2$  and  $e_g^2$  and a nondegenerate  $t_{2g}^1$  orbital [38]. Consistent with earlier DFT studies for bulk  $\text{CrI}_3$  [11–13] and as expected for ferromagnetic systems, the majority spin band is found at lower binding energies, while the minority spin channel gets almost completely depopulated due to large spin splitting. Interestingly, while the nondegenerate ground-state orbital is almost fully polarized, residual  $t_{2g}^2$  and  $e_g^2$  electronic states are found above the Fermi energy  $E_F = \omega = 0$ . As seen in Fig. 3, near  $E_F$  the valence and the conduction band of the

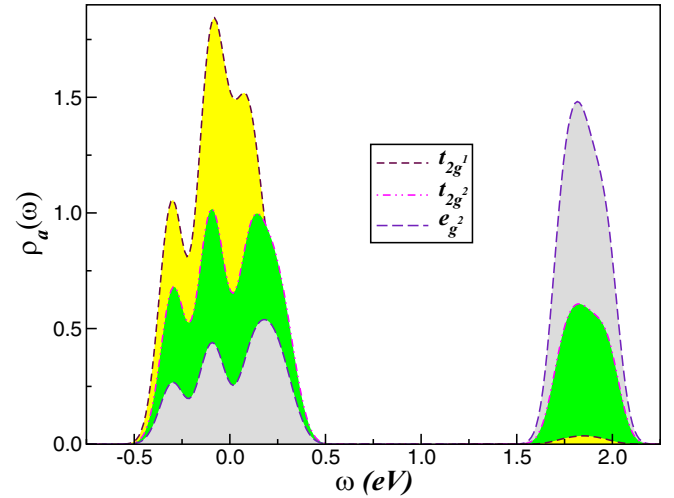


FIG. 4. Rhombohedral orbital-resolved GGA DOS of paramagnetic  $\text{CrI}_3$ , composed by twofold-degenerate  $t_{2g}^2$  and  $e_g^2$  orbitals and a nondegenerate  $t_{2g}^1$  orbital. An important feature to be seen is the narrow band bandwidth and the fact that all bands in GGA span a small region near  $E_F$ . This confirms that the electronic states relevant to  $\text{CrI}_3$  are the Cr  $3d$ -states.

majority spin channel are well separated, with a finite gap between them, characterizing the band-insulating state of ferromagnetic  $\text{CrI}_3$  [11]. Taken together, our GGA results in the main panels of Fig. 3 suggest strong spin-orbital differentiation in  $\text{CrI}_3$  which would lead to decreased electron correlation effects through increasing spin polarization. To confirm this aspect we show in the lower-inset of Fig. 3 the GGA+DMFT [24] result (see our discussion below) for ferromagnetic  $\text{CrI}_3$ , showing very similar total DOS as compared to the bare GGA result. The central result to be seen in this inset is the tinny band broadening modification observed in the GGA+DMFT DOS. Hence, due to strong spin-orbital polarization intrinsic MO dynamical correlations lead to weak spectral weight redistribution within the correlated MO electronic structure of ferromagnetic  $\text{CrI}_3$ .

According to our results in Fig. 3, the insulating state in ferromagnetic  $\text{CrI}_3$  is of orbital-selective type, where electronic localization is restricted to a particular subset of the active orbitals present in the problem. This tendency is clearly visible in Fig. 3, where the majority  $t_{2g}^1$  band is fully polarized, while in the  $t_{2g}^2$ - $\uparrow$  and  $e_g^2$ - $\uparrow$  channels conduction band states are found above  $E_F$ . Our results thus suggest the coexistence of distinct orbital degrees freedom in ferromagnetic  $\text{CrI}_3$  at low energies. Interestingly, in addition our GGA results in the upper inset of Fig. 3 shows nearly similar total DOS for the monoclinic ( $C2/m$ ) and the rhombohedral ( $R\bar{3}$ ) structural phases of paramagnetic  $\text{CrI}_3$ . This result implies weak bulk electronic structure reconstruction across the structural phase transition, and future spectroscopy studies are called for to corroborate the emergence of similar paramagnetic lineshapes in exfoliated  $\text{CrI}_3$  systems.

We now turn our attention to the bare electronic structure within the paramagnetic phase of rhombohedral  $\text{CrI}_3$ . Consistent with previous DFT calculations for the nonmagnetically ordered phase of  $\text{CrI}_3$  [11], our GGA results in Fig. 4 show

that the active electronic states in this chromium trihalide compound involve the Cr  $3d$  carriers, where all  $d$ -bands have appreciable weight near  $E_F$ . As seen, in the distorted  $R\bar{3}$  phase, the five Cr orbitals split into a nondegenerate  $t_{2g^1}$  band and two twofold-degenerate  $t_{2g^2}$  and  $e_g^2$  orbitals [38]. As common to transition-metal compounds, the  $e_g^2$  states are higher in energy and almost fully polarized within GGA. However, as shown below strong MO electron-electron interactions will scatter electrons among different orbital channels *via* the interorbital Coulomb interaction  $U'$  and the Hund's exchange parameter  $J_H$  [21], lowering the electronic  $e_g^2$  states towards the valence band and thus reducing the large GGA orbital polarization of paramagnetic CrI<sub>3</sub>. Importantly, the narrow bare bandwidth  $W$  near  $E_F$  (which is close to 1 eV for all active Cr orbitals) in GGA puts paramagnetic CrI<sub>3</sub> within Mott-localized family of strongly correlated transition-metal compounds [22].

Although first-principles GGA and GGA+ $U$  calculations have provided reliable structural and magnetic ground-state information for CrI<sub>3</sub> [7,11–13], they are known to generically fail to capture the ubiquitous dynamical correlation effects [22,25], and so cannot access MO Mott-localization and the emergence of Hubbard satellites (local moments) at high energies. Combining DFT with DMFT is the state-of-the-art prescription for overcoming this problem [25]. Thus, as common to correlated materials within GGA the one-electron part of the MO Hamiltonian for CrI<sub>3</sub> reads  $H_0 = \sum_{\mathbf{k},a,\sigma} \epsilon_a(\mathbf{k}) c_{\mathbf{k},a,\sigma}^\dagger c_{\mathbf{k},a,\sigma} + \sum_{i,a,\sigma} \epsilon_{i,a,\sigma} n_{i,a,\sigma}$ , where  $a = (t_{2g^1}, t_{2g^2}, e_g^2)$  denote its diagonalized  $3d$  orbitals and  $\epsilon_a(\mathbf{k})$  is the corresponding band dispersion, which encodes details of the one-electron band structure. These five Cr- $3d$  bands are the relevant one-particle inputs for MO-DMFT which generates a Mott-Hubbard insulating state as shown below. The many-body Hamiltonian for CrI<sub>3</sub> is  $H_{\text{int}} = U \sum_{i,a} n_{i,a,\uparrow} n_{i,a,\downarrow} + U' \sum_{i,a \neq b} n_{i,a} n_{i,b} - J_H \sum_{i,a \neq b} \mathbf{S}_{i,a} \cdot \mathbf{S}_{i,b}$ . (Here  $U$  is the on-site Coulomb interaction,  $U' = U - 2J_H$  is the interorbital Coulomb interaction term, and  $J_H$  is the Hund's coupling needed to describe superexchange coupling constants and magnetic interactions of Cr-based compounds, including CrI<sub>3</sub> [21]. To avoid double-counting of the (static) mean-field contributions from the electron-electron interactions already included in the DFT [39], the one-particle orbital energies are corrected from their bare GGA values to  $\epsilon'_{i,a,\sigma} = \epsilon_{i,a,\sigma} - U(n_{i,a,\sigma} - \frac{1}{2}) + \frac{1}{2}J_H(n_{i,a,\sigma} - 1)$  [36] so that  $H'_0 = \sum_{\mathbf{k},a,\sigma} \epsilon_{a,\sigma}(\mathbf{k}) c_{\mathbf{k},a,\sigma}^\dagger c_{\mathbf{k},a,\sigma} + \sum_{i,a,\sigma} \epsilon'_{i,a,\sigma} n_{i,a,\sigma}$ . We evaluate the many-particle Green's functions  $[G_{\mathbf{k},a,\sigma}(\omega)]$  of the MO Hamiltonian  $H = H'_0 + H_{\text{int}}$  within GGA+DMFT [25], using MO-iterated perturbation theory (MO-IPT) as impurity solver [40]. The DMFT solution involves replacing the lattice model by a self-consistently embedded MO-Anderson impurity model, and the self-consistency condition requiring the local impurity Green's function to be equal to the local Green's function for the lattice. The full set of equations for the MO-IPT case can be found in Ref. [40] so we do not repeat the equations here. This interpolative *ansatz* is known to account for the correct low- and high-energy behavior of the one-particle spectral function and self-energies of Hubbard-like models in the large- $D$  limit (DMFT). It ensures the Mott-Hubbard

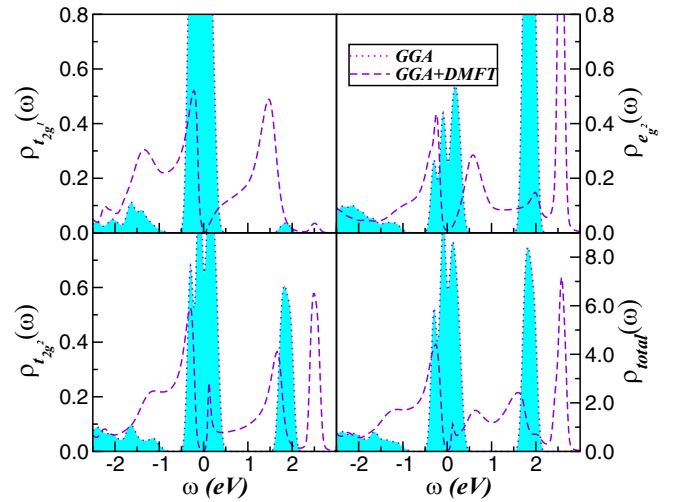


FIG. 5. Comparison between orbital-resolved and total GGA and GGA+DMFT(MO-IPT) [24] DOS for the Cr  $3d$ -orbitals of rhombohedral CrI<sub>3</sub>. Noteworthy is the electronic reconstruction and the formation of a Mott-Hubbard gap and Hubbard satellites at low and high energies, respectively, due to strong dynamical transfer of spectral weight within single-site DMFT approximation.

metal-insulator transition from a correlated metal to a Mott insulator as a function of the Coulomb interaction  $U$ . The MO-IPT scheme is computationally very efficient, with real frequency output at zero and finite temperatures [41], enabling the study of electronic structure reconstruction and transport properties of real materials with different magnetically ordered states and superconducting phase instabilities. Our real frequency MO-IPT scheme [40] has a proven record of good semiquantitative agreements with experiment for a range of correlated materials, and as shown recently it gives results for the spectral functions and self-energies in qualitatively accord with numerical exact continuous-time quantum Monte Carlo (CT-QMC) calculations [42,43], in spite of the fact that fully charged self-consistent DFT+DMFT calculations are presently unreachable within our perturbative treatment. In view of this, below we focus on the correlated spectral functions of paramagnetic CrI<sub>3</sub> bulk crystal and leave the extension of our approach as well as the derivation of the Mott-localized DFT+DMFT band structure for a future work.

Let us now discuss our GGA+DMFT(MO-IPT) result obtained within the Cr<sup>3+</sup> oxidation state in CrI<sub>3</sub> [3]. In Fig. 5 we display the effect of considering MO dynamical electron-electron interactions on the orbital-resolved spectral functions of the rhombohedral CrI<sub>3</sub> parent compound. As seen at fixed  $U$  values [24] and  $J_H = 0.85$  eV [11] the system is a true Mott-Hubbard insulator [21] where all orbital sectors display a Mott-Hubbard gap at  $E_F$  [22]. In spite of the orbital-selective transfer of spectral weight, the lower and upper Hubbard bands at high energies are visible in a more or less pronounced way, depending on the orbital character, in all orbital-resolved spectral functions. This behavior highlights the intrinsic tendency towards large transfer of spectral weight and Mott localization in transition-metal compounds [22] where the  $U/W$  ratio is usually sizable. Moreover, as seen in Fig. 5, paramagnetic CrI<sub>3</sub> is in the all-orbital Mott localized state

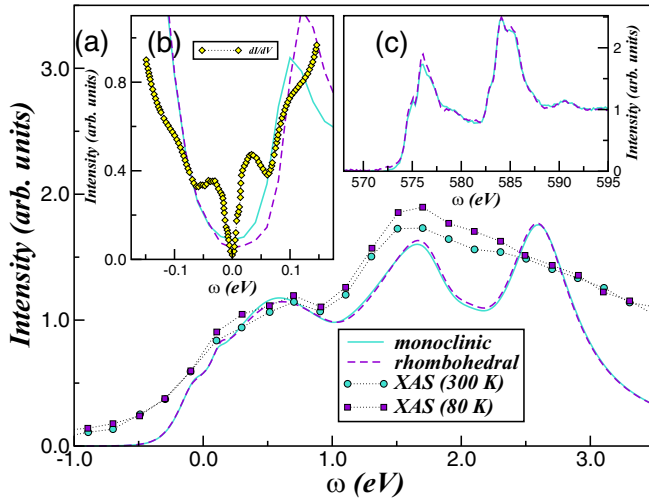


FIG. 6. Comparison between experimental XAS data and total GGA+DMFT(MO-IPT) DOS for the monoclinic (circles and solid line) and rhombohedral (squares and dashed line) structural phases of paramagnetic CrI<sub>3</sub>, showing in the main panel (a) the deconvoluted GGA+DMFT(MO-IPT) DOS using Lorentzian broadening. Notice the qualitative good theory experiment accord of the low-energy spectral lineshape. The right-inset (c) displays our experimental XAS results in the large energy window, showing good agreement with extant measurements [44] and confirming a bulk behavior that is nearly independent of crystal and band structure details: This intrinsic behavior is validated in the left inset (b), where the total GGA+DMFT(MO-IPT) spectral functions are also in good qualitative agreement with differential conductance of tetralayer CrI<sub>3</sub> [45] at energies above  $\pm 0.05$  eV, providing support to the view of orbital-dependent Coulomb correlation effects in CrI<sub>3</sub> [24].

with a narrow orbital-selective band-gap size followed by incoherent shoulder features relevant to low-energy optical and spectroscopy responses of paramagnetic CrI<sub>3</sub>.

Combining XAS measurements and GGA+DMFT calculations (see Fig. 6), we show that the electronic structure of paramagnetic CrI<sub>3</sub> needs to be described by localized *3d* orbitals, rather than itinerant states found in the bare GGA limit. It is interesting to notice in Fig. 5 that similar Mott localization can still occur in CrI<sub>3</sub> even if the on-site Coulomb interaction  $U$  is orbital-selective, as due to strong interorbital Mott mechanism, which equally blocks the hopping between the Cr sites. This peculiar behavior is caused by interorbital Coulomb correlation effects, so a single-site DMFT description is appropriate to CrI<sub>3</sub> and analogs. We also emphasize that the GGA+DMFT scheme used in this work can be applied to investigate the two-particle excitations probed, for example, in transport and NMR experiments.

In Fig. 6, we compare the GGA+DMFT spectral functions with XAS data obtained within the two structural phases of CrI<sub>3</sub> crystal. Interestingly and consistent with our GGA results in Fig. 3, our XAS results show weak electronic structure reconstruction over the entire energy range probed in experiment [see Fig. 6(c)], implying that the resonant absorption processes probed in by XAS is nearly independent of band and crystal structure details. This is corroborated by our theory-experiment comparison of the GGA+DMFT total DOS and

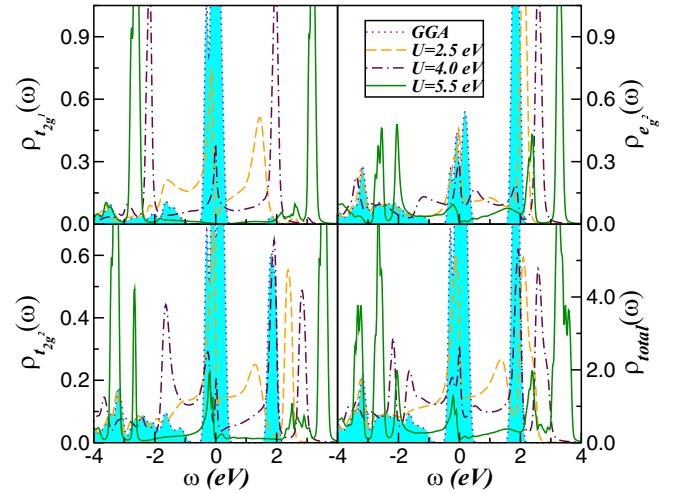


FIG. 7. Evolution of the GGA+DMFT(MO-IPT) orbital-resolved and total DOS of rhombohedral CrI<sub>3</sub> bulk crystal with increasing the on-site Coulomb interaction  $U (= U_{t_{2g}^1} = U_{t_{2g}^2} = U_{e_g^2})$ , showing all-electron Mott localization at  $U = 5.5$  eV. The bare GGA result is shown for comparison.

differential conductance through a tetralayer CrI<sub>3</sub> tunnel barrier [45], providing support for the electronic structure reconstruction in spite of our choice for the orbital-dependent Coulomb correlation effects [24]. It worth noticing, however, that since only the five *3d*-bands of CrI<sub>3</sub> were included in the GGA+DMFT treatment, in our theory-experiment comparison in the main panel of Fig. 6 we restrict the energy window up to 3.5 eV above  $E_F$ : this is beyond the region where only the five *d*-bands dominate in GGA. Clearly, good qualitative agreement with both XAS results is obtained at energies below 1.7 eV. In particular, the low-energy lineshape is faithfully reproduced. Remarkably, our GGA+DMFT calculations in Fig. 6(a) reproduce the two main low-energy features at 0.58 and 1.64 eV in good qualitative agreement with XAS results. Here, the double-bump features seen in XAS of CrI<sub>3</sub> are interpreted as arising from collective intra and interorbital fluctuations within the Mott-localized electronic state. Taken together, our results in Figs. 6(a) and 6(b), which display the theory-experiment comparison between GGA+DMFT total spectral function and differential conductance of tetralayer CrI<sub>3</sub> [45], constitute a consistent rationalization of basic one-particle responses of paramagnetic CrI<sub>3</sub> and serve as a basis to explore the MO electronic reconstruction of bulk and ultrathin Chromium trihalides [13,46].

What would be the electronic structure reconstruction in CrI<sub>3</sub> towards all-electron Mott localization if one assumes orbital-independent Coulomb interactions, i.e.,  $U_{t_{2g}^1} = U_{t_{2g}^2} = U_{e_g^2} = U$ ? To answer this question of fundamental importance in Fig. 7 we show the changes in the correlated spectra upon increasing the on-site Coulomb interaction  $U$ . As seen, while at  $U = 2.5$  eV the  $t_{2g}^1$  orbital is near to selective Mottness, an orbital-Kondo phenomena (characteristic of systems with orbital degeneracy) [36,47] develops within the  $t_{2g}^2$  and  $e_g^2$  orbital channels. Additionally, due to  $U'$ -induced orbital proximity effect, a Kondo-quasiparticle resonance also emerges at low energies in the  $t_{2g}^1$  orbital sector at  $U = 4.0$  eV, as

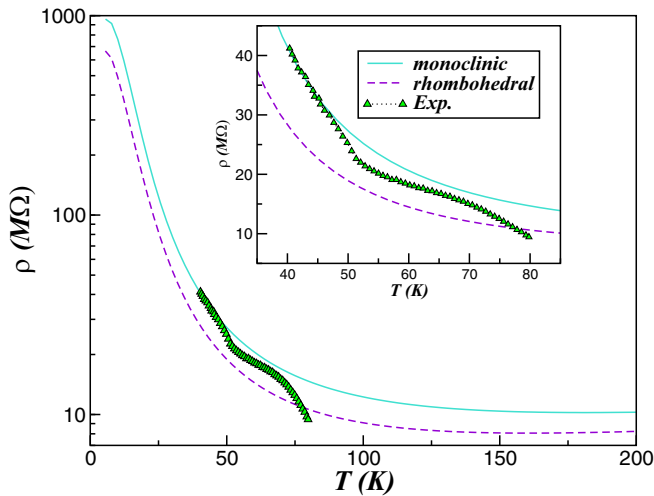


FIG. 8. Temperature dependence of the electrical resistivity of paramagnetic  $\text{CrI}_3$  bulk crystal obtained using GGA+DMFT(MO-IPT) spectral functions, showing its intrinsic insulating behavior as  $T \rightarrow 0$ : The theory curves have been rescaled in a way that  $\rho(T)$  for the monoclinic phase coincides with that of tetralayer  $\text{CrI}_3$  [45] at  $T = 40$  K. Inset shows the electrical resistivity within the experimental  $T$  range.

clearly seen in Fig. 7. Finally, due to strongly enhanced MO electronic interactions, at  $U = 5.5$  eV  $\text{CrI}_3$  is an all-electron Mott insulator, showing well-resolved Hubbard bands and Mott-Hubbard gaps. However, while the  $t_{2g}^1$  orbital is fully Mott localized, the double degenerated orbitals are close to selective Mottness, showing valence band low-energy shoulders. Taken together, strong dynamical correlations due to sizable  $U$  and  $U'$  cause appreciable spectral weight transfer over large energy scales, from low to high energies across the Mott metal-insulator transition, which leads to a drastic modification of the total spectral function as compared to that shown in Figs. 5 and 6, providing support to intrinsic orbital-selective Coulomb correlation effects in  $\text{CrI}_3$  [24].

As a further illustration for the correlated MO nature of paramagnetic  $\text{CrI}_3$ , in Fig. 8 we display the  $T$ -dependence of electrical resistivity [ $\rho_{dc}(T) \equiv 1/\sigma_{dc}(T)$ ], computed using the GGA+DMFT orbital-resolved spectral functions for the two structural phases of  $\text{CrI}_3$  in  $\sigma_{dc}(T)$  [42] assuming, as in Fig. 6, orbital-dependent Coulomb interaction effects. Various interesting features immediately stand out. First,  $\rho_{dc}(T \rightarrow 0)$  is large with clear insulating-like behavior above 40 K, in

accordance with the Mott-insulating description in Figs. 5 and 6. While deviations are expected to be seen below 40 K due to the onset of magnetic order, the detailed  $T$ -dependence between 40 and 46 K in Fig. 7 is similar to that reported in the experiment for tetralayer  $\text{CrI}_3$  [45]. A particularly interesting feature to be seen in Fig. 8 is the reduced resistivity for rhombohedral as compared to monoclinic  $\text{CrI}_3$ , a prediction which could be corroborated in future experimental observations.

### III. CONCLUSION

In this paper, we performed GGA+DMFT calculations for the multiorbital Hubbard model [21] to provide a microscopic description for the correlated electronic structure of  $\text{CrI}_3$  crystal. The central message of our approach is to show that a strong coupling [21] picture leads to a satisfying description for the insulating gap and the electronic structure reconstruction over the range of interest for experiments probing the excitation spectrum of the monoclinic and rhombohedral structural phases of  $\text{CrI}_3$ , showing good qualitative agreement with low-energy XAS data around the edge. Clearly, being based on a first-principles-correlated GGA+DMFT approach [25] involving realistic valence and conduction band electronic states of  $\text{CrI}_3$ , our proposal goes beyond earlier analytic calculations [21], which focused on superexchange coupling constants and magnetic interactions of Cr-based compounds. Taken together, our theory-experiment study provides support for the strongly correlated nature of  $\text{CrI}_3$  [7,21] and analogs [23] and it is expected to be generally applicable to understanding orbital-selective electronic structure reconstruction in strongly correlated electron systems and the underlying electronic state which might emerge in intrinsic van der Waals magnetic materials from bulk down to their two-dimensional limit [48].

### ACKNOWLEDGMENTS

L.C.'s work is supported by CNPq (Grant No. 304035/2017-3). Acknowledgement (L.C. and S.S.C.) is also made to CAPES. This research used resources of the Advanced Light Source, a U.S. DOE Office of Science User Facility under Contract No. DE-AC02-05CH11231. The work in Houston was supported, in part, by the State of Texas through the Texas Center for Superconductivity at the University of Houston.

- [1] H. H. Kim, B. Yang, S. Li, S. Jiang, C. Jin, Z. Tao, G. Nichols, F. Sfigakis, S. Zhong, C. Li, S. Tian, D. G. Cory, G.-X. Miao, J. Shane, K. F. Mak, H. Lei, K. Sun, L. Zhao, and A. W. Tsen, *Proc. Natl. Acad. Sci. USA* **116**, 11131 (2019).
- [2] J. Seo, D. Y. Kim, E. S. An, K. Kim, G.-Y. Kim, S.-Y. Hwang, D. W. Kim, B. G. Jang, H. Kim, G. Eom, S. Y. Seo, R. Stanina, M. Muntwiler, J. Lee, K. Watanabe, T. Taniguchi, Y. J. Jo, J. Lee, B. Il Min, M. H. Jo, H. W. Yeom, S.-Y. Choi, J. H. Shim, and J. S. Kim, *Sci. Adv.* **6**, eaay8912 (2020).
- [3] K. F. Mak, J. Shan, and D. C. Ralph, *Nat. Rev. Phys.* **1**, 646 (2019).

- [4] W. Jin, H. H. Kim, Z. Ye, S. Li, P. Rezaie, F. Diaz, S. Siddiq, E. Wauer, B. Yang, C. Li, S. Tian, K. Sun, H. Lei, A. W. Tsen, L. Zhao, and R. He, *Nat. Commun.* **9**, 1 (2018).
- [5] H. Li, S. Ruan, and Y.-J. Zeng, *Adv. Mater.* **31**, 1900065 (2019).
- [6] J. F. Dillon, Jr. and C. E. Olson, *J. Appl. Phys.* **36**, 1259 (1965).
- [7] P. Jiang, C. Wang, D. Chen, Z. Zhong, Z. Yuan, Z.-Y. Lu, and W. Ji, *Phys. Rev. B* **99**, 144401 (2019).
- [8] Z. Sun, Y. Yi, T. Song, G. Clark, B. Huang, Y. Shan, S. Wu, D. Huang, C. Gao, Z. Chen, M. McGuire, T. Cao, D. Xiao, W.-T. Liu, W. Yao, X. Xu, and S. Wu, *Nature* **572**, 497 (2019).

- [9] Z. Wang, I. Gutiérrez-Lezama, N. Ubrig, M. Kroner, M. Gibertini, T. Taniguchi, K. Watanabe, Ataç Imamoğlu, E. Giannini, and A. F. Morpurgo, *Nat. Commun.* **9**, 2516 (2018).
- [10] B. Huang, G. Clark, E. Navarro-Moratalla, D. R. Klein, R. Cheng, K. L. Seyler, D. Zhong, E. Schmidgall, M. A. McGuire, D. H. Cobden, W. Yao, D. Xiao, P. Jarillo-Herrero, and X. Xu, *Nature* **546**, 270 (2017); T. Song, X. Cai, M. W.-Y. Tu, X. Zhang, B. Huang, N. P. Wilson, K. L. Seyler, L. Zhu, T. Taniguchi, K. Watanabe, M. A. McGuire, D. H. Cobden, D. Xiao, W. Yao, and X. Xu, *Science* **360**, 1214 (2018).
- [11] O. Besbes, S. Nikolaev, N. Meskini, and I. Solovyev, *Phys. Rev. B* **99**, 104432 (2019).
- [12] V. K. Gudelli and G.-Y. Guo, *New J. Phys.* **21**, 053012 (2019).
- [13] H. Wang, V. Eyert, and U. Schwingenschlögl, *J. Phys.: Condens. Matter* **23**, 116003 (2011).
- [14] M. A. McGuire, H. Dixit, V. R. Cooper, and B. C. Sales, *Chem. Mater* **27**, 612 (2015).
- [15] Y. Liu and C. Petrovic, *Phys. Rev. B* **97**, 014420 (2018).
- [16] S. Djurdjiš-Mijin, A. Šolajić, J. Pešić, M. Šćepanović, Y. Liu, A. Baum, C. Petrovic, N. Lazarević, and Z. V. Popović, *Phys. Rev. B* **98**, 104307 (2018).
- [17] S. Jiang, L. Li, Z. Wang, K. F. Mak, and J. Shan, *Nat. Nanotechnol.* **13**, 549 (2018).
- [18] J. L. Ladno and J. Fernández-Rossier, *2D Materials* **4**, 035002 (2017).
- [19] T. Li, S. Jiang, N. Sivasdas, Z. Wang, Y. Xu, D. Weber, J. E. Goldberger, K. Watanabe, T. Taniguchi, C. J. Fennie, K. F. Mak, and J. Shan, *Nat. Mater.* **18**, 1303 (2019).
- [20] W.-B. Zhang, Q. Qu, P. Zhu, and C.-H. Lam, *J. Mater. Chem. C* **3**, 12457 (2015).
- [21] S. Feldkemper and W. Weber, *Phys. Rev. B* **57**, 7755 (1998).
- [22] M. Imada, A. Fujimori, and Y. Tokura, *Rev. Mod. Phys.* **70**, 1039 (1998).
- [23] I. Pollini, *Solid State Commun.* **106**, 549 (1998).
- [24] If not mentioned otherwise, in this work we consider orbital-selective  $U$  vales  $U_{t_{2g}^1} = 2.75$  eV and  $U_{t_{2g}^2} = U_{e_g} = 4.0$  eV to derive similar electronic reconstruction for active chromium channels within the paramagnetic phase of bulk  $\text{CrI}_3$ .
- [25] G. Kotliar, S. Y. Savrasov, K. Haule, V. S. Oudovenko, O. Parcollet, and C. A. Marianetti, *Rev. Mod. Phys.* **78**, 865 (2006).
- [26] L. Craco, S. S. Carara, and S. Leoni, *Phys. Rev. B* **99**, 045112 (2019).
- [27] J. M. Soler, E. Artacho, J. D. Gale, A. García, J. Junquera, P. Ordejón, and D. Sánchez-Portal, *J. Phys.: Condens. Matter* **14**, 2745 (2002); E. Artacho, E. Anglada, O. Dieguez, J. D. Gale, A. García, J. Junquera, M. Martín, P. Ordejón, J. M. Pruneda, D. Sánchez-Portal, and J. M. Soler, *ibid.* **20**, 064208 (2008).
- [28] J. P. Perdew, K. Burke, and M. Ernzerhof, *Phys. Rev. Lett.* **77**, 3865 (1996).
- [29] N. Troullier and J. L. Martins, *Phys. Rev. B* **43**, 1993 (1991).
- [30] W. Kohn and L. J. Sham, *Phys. Rev.* **140**, A1133 (1965).
- [31] J. Junquera, Ó. Paz, D. Sánchez-Portal, and E. Artacho, *Phys. Rev. B* **64**, 235111 (2001).
- [32] J. Moreno and J. M. Soler, *Phys. Rev. B* **45**, 13891 (1992).
- [33] H. J. Monkhorst and J. D. Pack, *Phys. Rev. B* **13**, 5188 (1976).
- [34] Z. Wu, J. Yu, and S. Yuan, *Phys. Chem. Chem. Phys.* **21**, 7750 (2019).
- [35] Y.-D. Chuang, X. Feng, A. Cruz, K. Hanzel, A. Brown, A. Spucce, A. Frano, W.-S. Lee, J. Kim, Y.-J. Chen, B. Smith, J. S. Pepper, Y.-C. Shao, S.-W. Huang, L. A. Wray, E. Gullikson, Z.-X. Shen, T. P. Devereaux, A. Tremisn, W. Yang, J. Guo, R. Duarte, and Z. Hussain, *J. Electron Spec. Rel. Phenomena* (2019), doi: 10.1016/j.elspec.2019.146897.
- [36] L. Craco, M. S. Laad, and E. Müller-Hartmann, *Phys. Rev. Lett.* **90**, 237203 (2003).
- [37] L. Craco, S. Leoni, M. S. Laad, and H. Rosner, *Phys. Rev. B* **76**, 115128 (2007).
- [38] The subscripts 1 and 2 denote the orbital degeneracy of the  $t_{2g}$  and  $e_g$  orbitals intrinsic to  $\text{CrI}_3$  [12].
- [39] See S. Sarkar and P. Kratzer, *Phys. Rev. Materials* **4**, 104006 (2020), and references therein.
- [40] L. Craco, *Phys. Rev. B* **77**, 125122 (2008).
- [41] M. S. Laad, L. Craco, and E. Müller-Hartmann, *Phys. Rev. B* **73**, 045109 (2006).
- [42] L. Craco and S. Leoni, *Phys. Rev. B* **100**, 121101(R) (2019).
- [43] L. Craco and S. Leoni, *Phys. Rev. B* **102**, 045142 (2020).
- [44] A. Frisk, L. B. Duffy, S. Zhang, G. van der Laan, and T. Hesjedal, *Materials Lett.* **232**, 5 (2018).
- [45] D. R. Klein, D. MacNeill, J. L. Lado, D. Soriano, E. Navarro-Moratalla, K. Watanabe, T. Taniguchi, S. Manni, P. Canfield, J. Fernández-Rossier, and P. Jarillo-Herrero, *Science* **360**, 1218 (2018).
- [46] H. H. Kim, B. Yang, S. Tian, C. Li, G.-X. Miao, H. Lei, and A. W. Tsen, *Nano Lett.* **19**, 5739 (2019).
- [47] P. Jarillo-Herrero, J. Kong, H. S. J. van der Zant, C. Dekker, L. P. Kouwenhoven, and S. De Franceschi, *Nature* **434**, 484 (2005).
- [48] K. S. Burch, D. Mandrus, and J.-G. Park, *Nature* **563**, 47 (2018).